J. Fluid Mech. (2007), *vol.* 580, *pp.* 359–380.
doi:10.1017/S0022112007005472 Printed in the United Kingdom

Buoyancy-driven crack propagation: the limit of large fracture toughness

S. M. ROPER† AND J. R. LISTER

Institute of Theoretical Geophysics, Department of Applied Mathematics and Theoretical Physics, Wilberforce Road, Cambridge, CB3 0WA, UK

(Received 12 May 2006 and in revised form 13 December 2006)

We study steady vertical propagation of a crack filled with buoyant viscous fluid through an elastic solid with large effective fracture toughness. For a crack fed by a constant flux Q, a non-dimensional fracture toughness $K = K_c/(3\mu Qm^3/2)^{1/4}$ describes the relative magnitudes of resistance to fracture and resistance to viscous flow, where K_c is the dimensional fracture toughness, μ the fluid viscosity and m the elastic modulus. Even in the limit $K \gg 1$, the rate of propagation is determined by viscous effects. In this limit the large fracture toughness requires the fluid behind the crack tip to form a large teardrop-shaped head of length $O(K^{2/3})$ and width $O(K^{4/3})$, which is fed by a much narrower tail. In the head, buoyancy is balanced by a hydrostatic pressure gradient with the viscous pressure gradient negligible except at the tip; in the tail, buoyancy is balanced by viscosity with elasticity also playing a role in a region within $O(K^{2/3})$ of the head. A narrow matching region of length $O(K^{-2/5})$ and width $O(K^{-4/15})$, termed the neck, connects the head and the tail. Scalings and asymptotic solutions for the three regions are derived and compared with full numerical solutions for $K \leqslant 3600$ by analysing the integro-differential equation that couples lubrication flow in the crack to the elastic pressure gradient. Time-dependent numerical solutions for buoyancy-driven propagation of a constant-volume crack show a quasi-steady head and neck structure with a propagation rate that decreases like $t^{-2/3}$ due to the dynamics of viscous flow in the draining tail.

1. Introduction

The transport of magma through the Earth's crust in fissures, or 'dykes', that propagate from a source region towards the surface has motivated many theoretical and experimental investigations of fluid-driven fracture in an elastic solid. Further motivation is provided by the use of hydrofracture to enhance oil recovery (e.g. Geertsma & Haafkens 1979; Detournay 2004; Garagash 2006) and by the propagation of water-filled crevasses in glaciers. Discussion of the geological background to modelling of dyke propagation can be found, for example, in the reviews by Pollard (1987), Rubin & Pollard (1987), Lister & Kerr (1991) and Rubin (1995); an introduction to hydrofracture is given in the monograph by Valko & Economides (1995).

In this paper we consider vertical propagation driven by the buoyancy of the fluid relative to the surrounding elastic solid. Weertman (1971*a*) noted that if the fluid pressure is hydrostatic then there is a critical height and volume of crack,

† Present address: Engineering Sciences and Applied Math, Northwestern University, Evanston, IL 60208–3125, USA.

set by a balance between buoyancy and fracture toughness, at which the condition for fracture propagation is just reached at the upper tip of crack and the width of the crack remains just positive at the lower tip. This led him to suggest that a teardrop-shaped pulse of magma, of this critical volume, could propagate upwards while maintaining the critical height by fracturing at the top and closing up at the bottom. This quasi-static model provides no prediction of the ascent velocity, and an attempt (Weertman 1971*b*) to incorporate the effects of fluid viscosity in a fixed-height pulse was largely unsuccessful owing to the fact, noted by Stevenson (1982), that it is impossible for a crack filled with viscous fluid to close completely at its tail.

A somewhat different picture is provided by travelling-wave solutions for steady fluid-driven propagation of a crack fed a constant flux of viscous fluid at depth (Spence, Sharpe & Turcotte 1987; Lister 1990). These calculations, which solve the fully coupled system of equations of viscous fluid dynamics, elasticity and linear elastic fracture mechanics (LEFM), describe a crack with a bulbous head of vertical scale set by a balance between buoyancy and elasticity and a long tail of uniform width set by a balance between buoyancy and viscosity. Lister (1990) showed that a conclusion of Spence *et al.* (1987), that there is only a solution for a dimensionless fracture toughness $K \approx 1.85$, was an unfortunate artifact of their numerical scheme, and calculated solutions for the range $0 \leqslant K \leqslant 2$. The propagation rate is thus set by the source flux, or crack width, in the tail.

There are two main reasons for re-examining this problem in the limit of large K. The first is the suggestion that the effective fracture toughness in lithospheric fracture may be much greater than that suggested by laboratory measurements on rock cores (Fialko & Rubin 1997) owing to extensive inelastic damage ahead of the crack tip and on either side of the fracture plane in geological situations (see e.g. Andrews & Emelius 1975; Delaney *et al.* 1986; Rubin 1993; Meriaux *et al.* 1999). The other is the stimulus provided by a large number of experimental studies of fluid-driven crack propagation in gelatin or polyacrylamide gel (e.g. Fiske & Jackson 1972; Takada 1990; Lister & Kerr 1991; Muller, Ito & Martel 2001; Ito & Martel 2002; Heimpel & Olson 1994; Menand & Tait 2002), which have a sufficiently small shear modulus to deform significantly on a laboratory scale. These experiments, intended as laboratary analogues of geological situations, typically involve the injection of buoyant fluid from a source at the base of the solid, with the flux of fluid controlled either by injecting a fixed volume (e.g. Takada 1990; Muller *et al.* 2001; Ito & Martel 2002) or by keeping the source at a constant overpressure (e.g. Menand & Tait 2002). Some are designed to examine additional effects such as the interaction of a number of cracks (Takada 1990; Ito & Martel 2002) or the effects of pre-existing stress variations in the solid (Muller *et al.* 2001). Both these studies and simpler studies of vertical rise of a single fluid-filled crack observe that laboratory-scale buoyant cracks resemble the Weertman pulse with almost all the fluid in a large teardrop-shaped head and only a very thin trailing tail. In this paper we show that this structure can be explained by propagation with a large dimensionless fracture toughness K, but that the propagation rate is still controlled viscously by the flux from the tail.

In order to elucidate this coupling between viscous flow in the tail and propagation of the head, we consider two simple model problems which encapsulate the essential mechanisms. Many of the complications in dyke propagation are neglected, in particular, the possibility of volatile exsolution in a tip cavity (Anderson 1978; Lister 1990), interaction with pore fluids in the surrounding rock (Ruina 1978; Rubin 1998) and solidification or melting at the dyke walls (Lister 1994*a*, *b*). It is also assumed that the zone of inelastic damage near the crack tip is sufficiently localized that it can

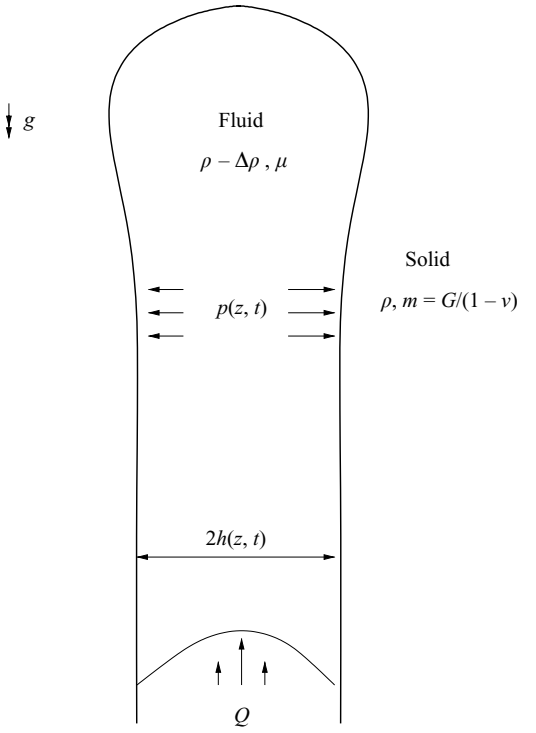

FIGURE 1. Definition sketch. A constant flux Q of buoyant fluid feeds a steadily propagating crack of width $2h(z, t)$, which generates an elastic pressure p_e.

be described in the context of LEFM by an effective fracture toughness (Kanninen & Popelar 1985).

We begin with analysis of steady propagation of a crack fed by a constant flux of fluid in the limit $K \gg 1$. This problem is formulated and the governing equations non-dimensionalized in § 2. Numerical solutions over the range $2 \leqslant K \leqslant 16$ are used in § 3 to motivate a rescaling of the equations that is appropriate for $K \gg 1$. The rescaled equations are solved numerically for values of K up to 3600. It is shown that the solution splits into three major asymptotic regions — a head, tail and neck — with different scalings and physical balances in each. The features of the solution in each of these regions are analysed and explained in §§ 4.1, 4.2 and 5, respectively.

In § 6 we present calculations of the time-dependent propagation of a finite volume of fluid. The solution structure again exhibits a head, neck and tail, but the width of the tail is now time-dependent and non-uniform and, as a result, the propagation rate decreases with time; the head and neck are seen to be the elastic resolution of the shock structure that would otherwise develop from the viscous–buoyancy balance in the tail. Discussion of these results and their geological and laboratory applications is presented in § 7.

2. Formulation

Consider steady propagation of a planar two-dimensional crack filled with fluid of viscosity μ and density $\rho - \Delta\rho$ through an infinite uniform impermeable elastic solid of shear modulus G, Poisson's ratio ν and apparent density $\rho = (1/g)\mathrm{d}\sigma_{xx}/\mathrm{d}z$ (figure 1), where σ_{xx} is the ambient stress normal to the crack plane prior to crack

propagation. (The apparent density ρ is equal to the true density for the simple case of a solid with an isotropic stress in gravitational equilibrium, but the definition given here allows for geological situations in which the ambient horizontal stresses deviate from 'lithostatic' owing to regional tectonic deformation.)

We suppose that the crack propagates vertically due to the buoyancy $\Delta\rho\, g$ of the fluid relative to the solid, and is fed at depth by a constant fluid flux Q. Let the half-width of the crack be $h(z, t)$ for $-\infty < z < z_n(t)$, where the crack tip is at $z = z_n(t)$ and z is the vertical coordinate. The resistance of the solid to fracture is assumed to be measured by the fracture toughness, or critical stress intensity, K_c (Irwin 1958; Lawn & Wilshaw 1975). The derivation of the governing equations for this situation is described in detail in both Spence *et al.* (1987) and Lister (1990), and is therefore given only briefly below.

The flow is driven by a combination of the fluid buoyancy $\Delta\rho\, g$ and an elastic pressure $p_e(z, t)$ associated with the deformation of the solid due to the dilation of the crack. Standard results from lubrication theory and linear elasticity give the coupled system

$$\frac{\partial h}{\partial t} = \frac{1}{3\mu}\frac{\partial}{\partial z}\left(h^3\left(\frac{\partial p_e}{\partial z} - \Delta\rho\, g\right)\right), \tag{2.1}$$

$$p_e(z) = -\frac{m}{\pi}\int_{-\infty}^{z_n} \frac{\partial h}{\partial s}\frac{1}{s - z}\,\mathrm{d}s, \tag{2.2}$$

for h and p_e, where $m = G/(1 - \nu)$. The fracture criterion that the stress intensity at the crack tip is equal to the critical value K_c can be written as

$$h \sim \frac{K_c}{m}[2(z_n - z)]^{1/2} \quad \text{as } z \to z_{n-}. \tag{2.3}$$

We search for steadily propagating solutions in which far from the crack tip the crack width tends to a constant and the elastic pressure gradient tends to zero. The far-field half-width h_∞ and the steady propagation rate c are then related to the source flux Q by

$$h_\infty = \left(\frac{3\mu Q}{2\Delta\rho\, g}\right)^{1/3}, \qquad c = \frac{Q}{2h_\infty} = \left(\frac{Q^2\Delta\rho\, g}{12\mu}\right)^{1/3}. \tag{2.4}$$

Transforming to a frame $x = z_n(0) + ct - z$ moving with the crack tip, we can integrate (2.1) and use $h = 0$ at $x = 0$ to obtain

$$3\mu c = h^2\left(\frac{\partial p_e}{\partial x} + \Delta\rho g\right). \tag{2.5}$$

Equations (2.5), (2.2) and (2.3) are non-dimensionalized with respect to the scales

$$\hat{x} = \left(\frac{mh_\infty}{\Delta\rho\, g}\right)^{1/2}, \qquad \hat{h} = h_\infty, \qquad \hat{p} = \frac{m\hat{h}}{\hat{x}}, \qquad \hat{K} = \hat{p}\hat{x}^{1/2}, \tag{2.6}$$

to obtain

$$p' = \frac{1}{h^2} - 1, \tag{2.7}$$

$$p(x) = -\frac{1}{\pi}\int_0^\infty \frac{h'(s)}{s - x}\,\mathrm{d}s, \tag{2.8}$$

$$h(x) \sim K(2x)^{1/2} \quad \text{as } x \to 0^+, \tag{2.9}$$

where

$$K = \left(\frac{2K_c^4}{3\mu Q m^3} \right)^{1/4} \tag{2.10}$$

is the dimensionless fracture toughness. In geological applications $\hat{h}$ is tens of centimetres and $\hat{x}$ is a few kilometres, so that the crack is long and thin as assumed. The main focus of this paper is the solution of (2.7)–(2.9) for $K \gg 1$.

For the numerical schemes, we note that (2.8) can be inverted to give (Spence *et al.* 1987)

$$h(x) = \frac{1}{\pi} \int_0^\infty k(s, x) p'(s)\, \mathrm{d}s, \quad \text{where } k(s, x) = (x - s) \log \left| \frac{s^{1/2} + x^{1/2}}{s^{1/2} - x^{1/2}} \right| - 2(xs)^{1/2}. \tag{2.11}$$

Using the asymptotic form $k \sim -4(sx)^{1/2}$ for $x \ll s$, we can also reformulate (2.9) as

$$\int_0^\infty s^{1/2} p'(s)\, \mathrm{d}s + \frac{\pi K}{\sqrt{8}} = 0. \tag{2.12}$$

3. Numerical solution for moderate K

Lister (1990) reported solutions to (2.7)–(2.9) for $0 \leqslant K \leqslant 2$, over which range there was little variation in the crack shape with K. In order to identify the trends for large K, we used the same numerical method (though with $N = 300$ panels instead of 100) to obtain solutions up to $K = 16$.

3.1. *Variation for* $0 \leqslant K \leqslant 16$

All solutions show a head-and-tail structure (figure 2) in which there is a bulbous head behind the crack tip and then a tail in which the half-width $h \approx 1$. For $K < 2$ the length of the head varies little with K (figure 2*a*) and the width is comparable with that of the tail. However, for $K > 2$ the length and width of the head increase significantly with K (figure 2*b*). The minimum width, which occurs in a neck between the head and tail, decreases as K increases. The shape of the head for $K = 4$, 8 and 16 is similar though on different scales.

The profiles of $p'(x)$ have a positive singularity as $x \to 0^+$, as noted by Spence *et al.* (1987) from (2.7) with $h \to 0$. For the larger values of K, a broad region where $p' \approx -1$ develops through the rest of the head (figure 2*c*), which is followed by a narrow peak in the neck and then decay towards $p' \approx 0$ in the tail. That $p' \approx -1$ in the head for $K \gg 1$ is a consequence of $h \gg 1$ and corresponds to a dominant balance between buoyancy and a hydrostatic pressure gradient.

The peak in p' between the head and the tail (figure 2) becomes less well-resolved as K increases owing to the point distribution in the numerical scheme of Lister (1990). Much better resolution is achieved below by rescaling the governing equations and modifying the numerical scheme to deal explicitly with large K.

3.2. *Scalings for* $K \gg 1$

From the results above we deduce that for $K \gg 1$ there is a head in which $p' \approx -1$ and a tail where $p' \to 0$. From (2.12) we estimate that the length scale L of the head is given by $L^{3/2} \sim K$. From (2.11) with $p' \sim -1$ over a region of size L we estimate that

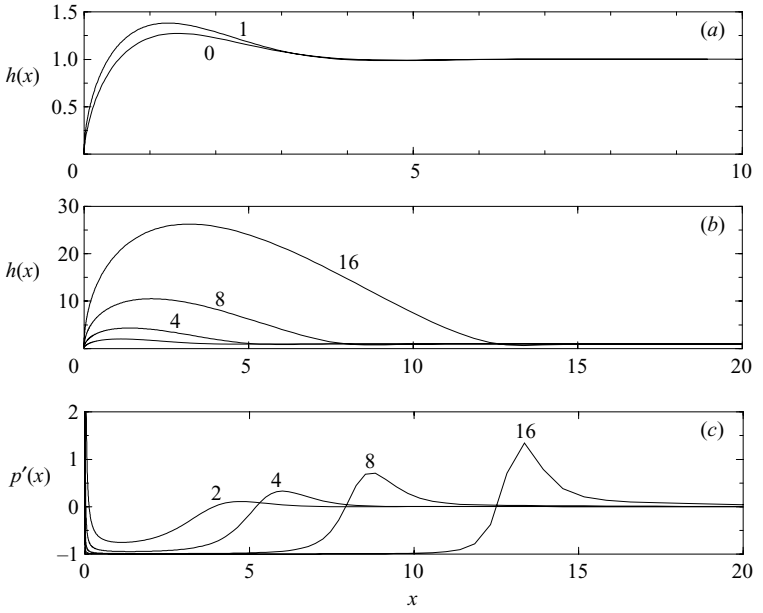

FIGURE 2. The half-width $h(x)$ for (*a*) $K=0$ and 1 (*b*) $K=2$, 4, 8 and 16. (*c*) The pressure gradient $p'(x)$ for $K=2$, 4, 8 and 16. The profiles of $h(x)$ show a head-and-tail structure for all values of K. As K increases beyond 2 the head grows significantly in length and width, and becomes characterized by $p' \approx -1$.

$h \sim L^2 \sim K^{4/3}$. If $p' \sim 1$ then $p \sim L \sim K^{2/3}$. These arguments motivate the rescaling

$$X = \frac{x}{K^{2/3}}, \qquad H = \frac{h}{K^{4/3}}, \qquad P = \frac{p}{K^{2/3}}, \qquad \frac{\mathrm{d}P}{\mathrm{d}X} = \frac{\mathrm{d}p}{\mathrm{d}x} \tag{3.1}$$

after which the governing equations become

$$P' = \frac{1}{K^{8/3}H^2} - 1, \qquad H = \frac{1}{\pi}\int_0^\infty k(S,X)P'\,\mathrm{d}S, \qquad \int_0^\infty S^{1/2}P'\,\mathrm{d}S + \frac{\pi}{\sqrt{8}} = 0. \tag{3.2a–c}$$

Note that the constant far-field half-width $h(\infty)=1$ becomes $H(\infty)=K^{-4/3}$.

The rescaled equations (3.2) were solved using a modified numerical scheme, which is described in detail in Appendix A. Numerical solutions for the rescaled variables $H(X)$ and $P'(X)$ for $2 \leqslant K \leqslant 32$ are shown in figure 3.

As K increases, the shape of the head tends to an $O(1)$ limit, confirming the above scaling arguments. The head appears to ocuppy the region $0 \leqslant X \leqslant 2$, outside of which the half-width is no more than the $O(K^{-4/3})$ far-field width. Though H becomes small in the tail, P' remains $O(1)$ at fixed X (with $P' \to 0$ as $X \to \infty$). The neck is characterized by a peak in P' of decreasing width and increasing height. These observations motivate the following analysis.

4. Analysis of the head and tail

In this section we derive asymptotic solutions for the head and tail as $K \to \infty$. Discussion of the neck is deferred to § 5.

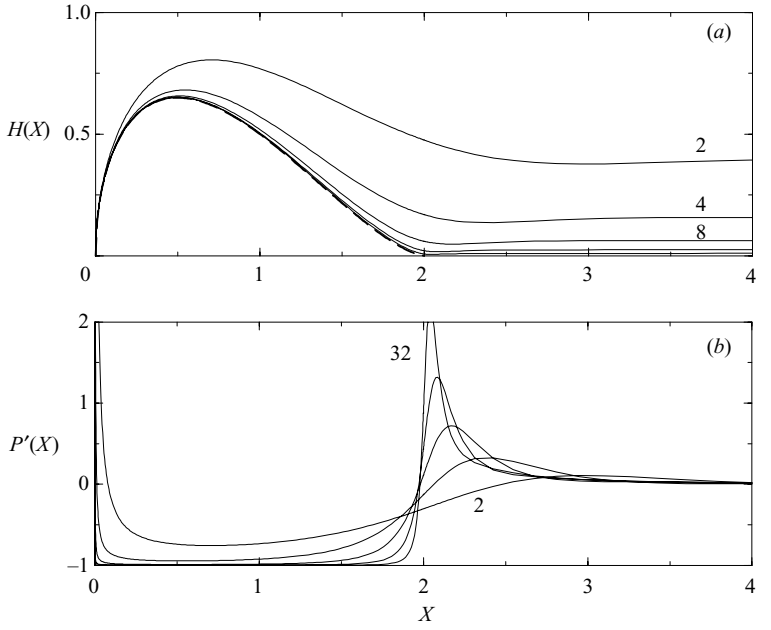

FIGURE 3. Solutions of (3.2) for $K = 2$, 4, 8, 16 and 32: (*a*) $H(X)$; (*b*) $P'(X)$. As K increases, $H(X)$ tends to the analytic solution $H_0 = \frac{1}{2}X^{1/2}(2-X)^{3/2}$ (dashed, (4.8*a*)) and $P' \to -1$ in the head $0 < X < 2$.

4.1. *The head*

We assume that, as $K \to \infty$, $H = O(1)$ only in a finite region $0 \leqslant X \leqslant L_h$ (where we hope to show $L_h = 2$) and $H \to 0$ outside this region. The asymptotic solution to (3.2) as $K \to \infty$ is thus the solution to

$$P' = -1 \quad \text{if } 0 \leqslant X \leqslant L_h, \tag{4.1}$$

$$H = 0 \quad \text{if } X \leqslant 0 \text{ or } X \geqslant L_h, \tag{4.2}$$

$$P = -\frac{1}{\pi}\int_0^{L_h} \frac{H'(S)\,\mathrm{d}S}{S-X}, \tag{4.3}$$

$$H \sim (2X)^{1/2} \quad \text{as } X \to 0, \tag{4.4}$$

$$H' = 0 \quad \text{at } X = L_h. \tag{4.5}$$

Equation (4.4) is equivalent to (3.2*c*), and (4.5) is a condition that H closes smoothly at $X = L_h$ to match to the constant width of the tail. From (4.1) we deduce that $P = c_0 - X$ for some constant c_0. By inversion of the Hilbert transform (4.3) subject to (4.2), we obtain

$$H = X^{1/2}(L_h - X)^{1/2}\left(c_0 + \frac{L_h}{4} - \frac{X}{2}\right). \tag{4.6}$$

The conditions (4.4) and (4.5) then imply that $c_0 = L_h/4$ and

$$L_h = 2, \tag{4.7}$$

as expected. Figure 3(*a*) shows good agreement between this asymptotic solution for $H(X)$ as $K \to \infty$ (dashed curve) and numerical solutions for moderately large values of K.

The $O(1)$ deformation in the head creates $O(1)$ elastic stresses in $X > 2$ even though H is $o(1)$ there. These stresses can be obtained by substitution of (4.6) into (4.3). We denote the asymptotic solution for H as $K \to \infty$ by H_0 and the corresponding elastic pressure by P_0, where

$$H_0 = \frac{1}{2}X^{1/2}(2-X)^{3/2}, \quad P_0 = \frac{3}{2} - X, \quad P_0' = -1 \quad \text{if } 0 \leqslant X < 2, \tag{4.8a–c}$$

$$H_0 = 0, \quad P_0 = \frac{3}{2} - X + \frac{(2X-1)(X-2)^{1/2}}{2X^{1/2}}, \quad P_0' = -1 + \frac{(2X^2-2X-1)}{2(X-2)^{1/2}X^{3/2}} \quad \text{if } X > 2. \tag{4.9a–c}$$

Both H_0 and P_0 are continuous at $X = 2$; the singularity in P_0' at $X = 2^+$ requires resolution by the neck.

4.2. *The tail in $X = O(1)$, and an $O(K^{-4/3})$ correction to the head*

For $2 < X \ll K^{4/3}$ the elastic pressure is dominated by the contribution P_0 from the head. (As noted in Appendix B, P_0 decays like X^{-2} for $X \gg 1$ and the contribution to P from the tail only becomes comparable when $X = O(K^{4/3})$.) Substitution of $P \sim P_0$ into the lubrication equation (3.2a) gives the shape of the tail as $H \sim K^{-4/3}H_{4/3}$, where

$$H_{4/3}(X) = \frac{1}{(1+P_0')^{1/2}} = \frac{2^{1/2}X^{1/4}(X-2)^{3/4}}{(2X^2-2X-1)^{1/2}} \quad \text{for } X > 2. \tag{4.10}$$

The width in the tail is thus $O(K^{-4/3})$ and the length scale in (4.10) is $O(1)$. Hence from (3.2b) the deformation in the tail generates an $O(K^{-4/3})$ contribution to the pressure gradient as a correction to P_0'. This suggests that

$$P' = P_0' + K^{-4/3}P_{4/3}' + O\left(K^{-8/3}\right), \tag{4.11}$$

$$H = H_0 + K^{-4/3}H_{4/3} + O\left(K^{-8/3}\right), \tag{4.12}$$

where H_0 and P_0' are given by (4.8) and (4.9). Note that $H_0 = 0$ in $X > 2$.

In the head $H = O(1)$ and so, from (3.2a), $P' + 1 = O(K^{-8/3})$. Thus

$$P_{4/3}' = 0 \quad \text{for } X < 2. \tag{4.13}$$

Equations (4.13) and (4.10) give $P_{4/3}'$ for $X < 2$ and $H_{4/3}$ for $X > 2$. Together with the integral equation (3.2b), they define a mixed problem that determines $P_{4/3}'$ in $X > 2$ and $H_{4/3}$ in $0 \leqslant X < 2$. Since the stress-intensity condition (3.2c) is met exactly by H_0, the appropriate boundary condition on $H_{4/3}$ is $H_{4/3} = O(X^{3/2})$ as $X \to 0^+$. The mixed problem was solved numerically using a scheme similar to that for the full problem.

Figure 4 compares the solution for $H_{4/3}$ with calculations of $K^{4/3}(H - H_0)$ from the full problem over the range $40 \leqslant K \leqslant 3600$. (Note that $H_0 = 0$ in $X > 2$.) We see that both the correction to H_0 in the head and the full solution H in the tail are well-described by $H_{4/3}$, though there is some kind of singular behaviour in the neck region $X \approx 2$.

Figure 5 examines the neck in more detail for $K \geqslant 160$. The full solution matches to the leading-order tail solutions P_0' and $H_{4/3}$ as X increases beyond 2. However, there is a region of disagreement around $X = 2$, which decreases in length as K increases and acts to bridge the very different behaviour in $X < 2$ and $X > 2$.

5. Analysis of the neck, $X \approx 2$

In the preceding section, we obtained analytical or numerical solutions for the $O(1)$ and $O(K^{-4/3})$ terms in (4.12) in both the head and the tail. The need for an

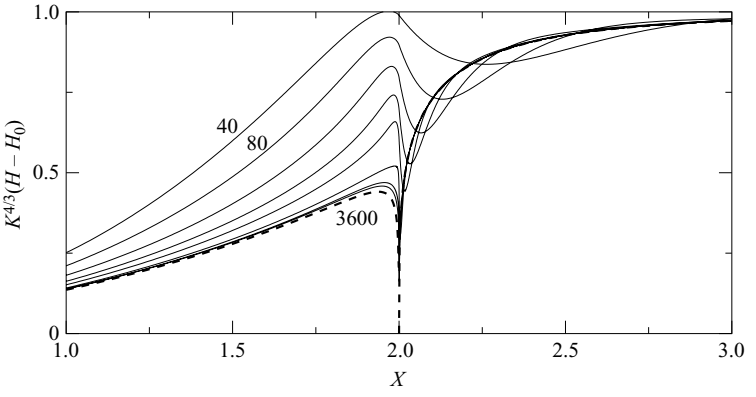

FIGURE 4. Plot of $K^{4/3}(H-H_0)$ against X for $K=40$, 80, 160, 320, 640, 1280, 2560 and 3600. The dashed curve is the theoretical prediction $H_{4/3}$ given by (4.10) in $X>2$ and by numerical solution of a mixed problem in $X<2$.

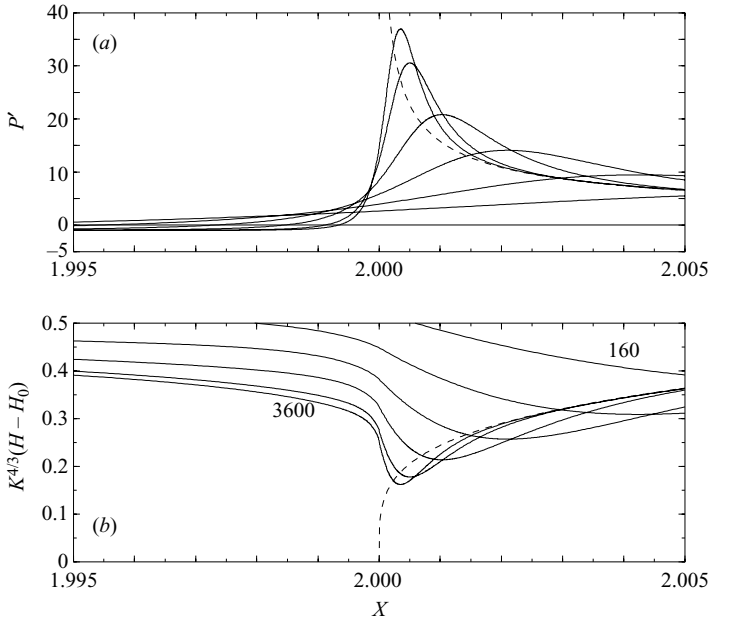

FIGURE 5. Plot of P' (a) and $K^{4/3}(H-H_0)$ (b) against X in the neck region for $K=160$, 320, 640, 1280, 2560 and 3600. As K increases, the peak pressure gradient increases, the minimum half-width decreases, and the length scale of the peak and minimum decreases. The theoretical predictions P_0' and $H_{4/3}$ (dashed) from (4.9a–c) and (4.10) give the leading-order behaviour away from $X=2$ as $K\to\infty$.

intermediate neck region that matches the head to the tail is a consequence of the breakdown of the asymptotic series (4.12) as $X=2$ is approached from either the head or the tail. In order to gain some understanding of the scalings in the neck, we examine the breakdown of the leading-order approximations as $X\to 2$.

5.1. *Approach from the tail*

The leading-order width $H_{4/3}$ in the tail was derived from the lubrication equation using the assumption that P' is dominated by the contribution P_0' from the head.

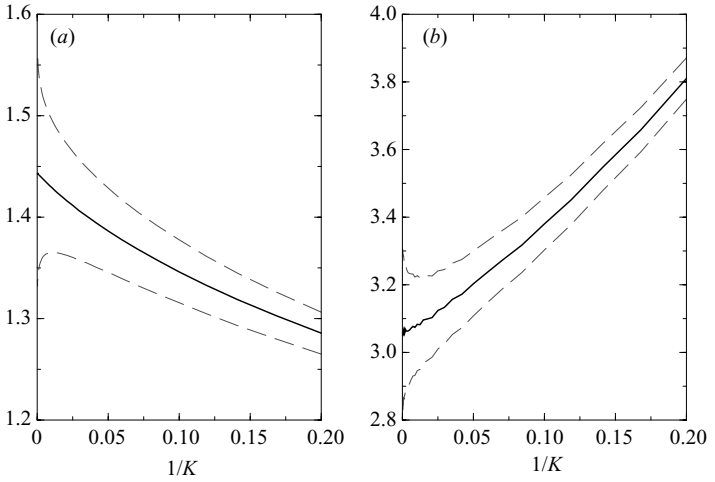

FIGURE 6. (*a*) Plot of $K^{8/5}H_{\min}$ (solid) and $K^{8/5\pm0.01}H_{\min}$ (dashed) against $1/K$. (*b*) Plot of $K^{16/15}L_{\min}$ (solid) and $K^{16/15\pm0.01}L_{\min}$ (dashed) against $1/K$. The length scale $L_{\min}$ is defined as $(2H_{\min}/H'')^{1/2}$, where the curvature H'' is evaluated at $H_{\min}$. The plots show that the scalings $H_{\min}\sim K^{-8/5}$ and $L_{\min}\sim K^{-16/15}$ suggested by (5.3) and (5.4) are correct.

However, $H_{4/3}\sim[\frac{8}{9}(X-2)]^{1/4}$ as $X\to 2^+$ and this singularity in $H_{4/3}$ implies a strong singularity in $P'_{4/3}$. Hence there is a growing contribution to P' from the local deformation as $X\to 2$ from the tail.

To understand this contribution, consider the model problem

$$h=x^{1/4}\quad\text{if } x\geqslant 0,\qquad p'=0\quad\text{if } x\leqslant 0,\qquad p(x)=-\frac{1}{\pi}\int_{\infty}^{\infty}\frac{h'(s)}{s-x}\,\mathrm{d}s. \tag{5.1a–c}$$

It is easy to show (see e.g. Erdelyi *et al.* 1954, p. 243 *et seq.*) that the solution is

$$h=(-4x)^{1/4}\quad\text{for } x\leqslant 0,\qquad p'=\tfrac{3}{16}x^{-7/4}\quad\text{for } x\geqslant 0. \tag{5.2}$$

Hence we expect the deformation $H_{4/3}$ in the tail to make a contribution to the elastic pressure gradient proportional to $K^{-4/3}(X-2)^{-7/4}$ as $X\to 2^+$. This contribution is of the same order as $P'_0\sim(X-2)^{-1/2}$ when

$$X-2\sim K^{-16/15} \tag{5.3}$$

at which scale

$$H\sim\frac{(X-2)^{1/4}}{K^{4/3}}\sim K^{-8/5}\quad\text{and}\quad P'\sim K^{8/15}. \tag{5.4}$$

The above argument suggests that the length scale and half-width of the neck decrease like $K^{-16/15}$ and $K^{-8/5}$, respectively, as $K\to\infty$. In order to test these scalings against our numerical solutions, we used a local quadratic fit in the neck to find the minimum half-width $H_{\min}$ and the curvature H'' at the minimum $X=X_{\min}$. The length scale of the neck was then estimated by $L_{\min}=(2H_{\min}/H'')^{1/2}$. Figure 6 shows plots of $H_{\min}$ and $L_{\min}$ and confirms the scalings proposed above; the scaling for P' follows from the scaling for H and also agrees with the numerical results. Figure 7 shows the rescaled shape of the neck; the collapse of the profiles is another indication that the solution in the neck is scaled correctly.

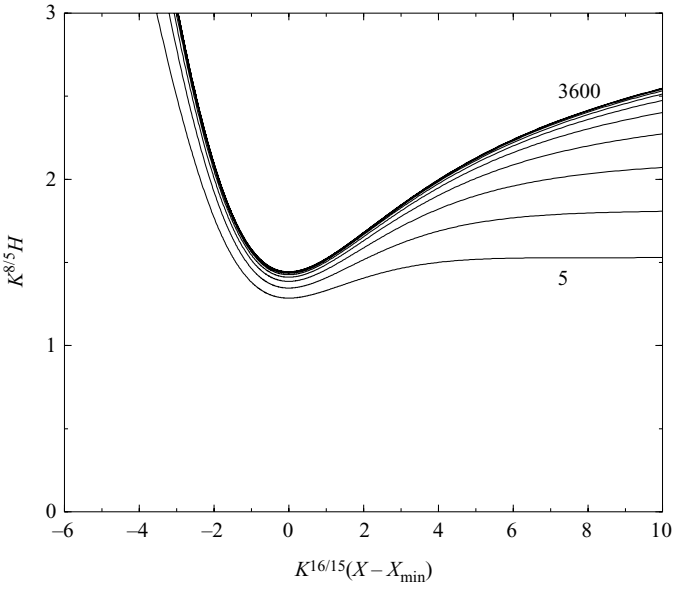

FIGURE 7. Plot of $K^{8/5}H$ against $K^{16/15}(X - X_{\min})$ for $K = 5$, 10, 20, ..., 2560 and 3600, where $X_{\min} \approx 2$ is the location of the minimum width $H_{\min}$ in the neck.

5.2. *Approach from the head*

The leading-order solution in the head is $H_0 = \frac{1}{2}X^{1/2}(2 - X)^{3/2}$ and $P_0' = -1$, which is based on the assumption that $H = O(1)$. This assumption breaks down as $X \to 2^-$, giving rise to two problems with the asymptotic series (4.12). First, from (5.1*a*) we expect the correction $H_{4/3}$ to scale like $(2 - X)^{1/4}$ as $X \to 2^-$. Hence $H_0 \sim K^{4/3}H_{4/3}$ when $2 - X \sim K^{-16/15}$ and $H \sim (2 - X)^{-8/5}$, which are the same scalings as from the approach from the tail.

Second, from the lubrication equation (3.2*a*) we note that P' can no longer be approximated by -1 when

$$\frac{1}{K^{8/3}H^2} \sim 1. \tag{5.5}$$

Based on the behaviour of H_0 as $X \to 2^-$, this seems likely to occur when $(2 - X) \sim K^{-8/9}$, which is a (slightly) greater length scale than $K^{-16/15}$. So, as the neck is approached from the head, we expect to see significant non-hydrostatic pressure gradients on this length scale, generated by the lubrication flow in the thin gap at the base of the teardrop-shaped head. The numerical solutions do show non-hydrostatic pressure gradients on a length scale slightly greater than the $K^{-16/15}$ scale of the neck but, owing to the similarity of the exponents and the lack of any clearly defined quantifiable feature of this region, it has not been possible to confirm that the scaling is $K^{-8/9}$ from a plot similar to figure 6.

As discussed further in Appendix C, we have also been unable to formulate an inner problem to determine the limiting scaled neck shape of figure 7. We conclude that there is a neck, with scales $K^{-16/15}$ and probably $K^{-8/9}$, that matches the head to the tail. Fortunately, as shown in the following section, it does not seem necessary to solve for the neck in order to understand how the dynamics of the head and tail determine the evolution of a time-dependent problem.

6. Finite-volume release

Up to this point we have been considering steady propagation of a crack fed by a constant flux of fluid at depth. This analysis can be adopted to calculate unsteady propagation in circumstances where the overall vertical scale of the crack is much greater than the vertical scale of the Weertman (1971*a*) pulse. The simplest example of such a time-dependent problem is vertical propagation of a crack containing a constant volume of fluid.

Spence & Turcotte (1990) presented an approximate solution to this problem in which the elastic pressure gradient was neglected in (2.1) so that propagation was governed by a simple balance between buoyancy and the viscous pressure drop. With p_e set to zero, (2.1) can be solved by the method of characteristics for any initial conditions, and the solution tends towards a self-similar form in which there is a frontal shock with h non-zero at $z = z_n(t)$. Spence & Turcotte (1990) suggested that the frontal shock should be resolved by matching to a near-tip solution in which elastic pressures and fracture resistance would need to be reintroduced, but did not proceed further. Rubin (1998) presented numerical calculations including the elastic pressures and fracture resistance, which confirmed the hypothesis of Spence & Turcotte (1990) and showed that the near-tip solution resembles the Weertman pulse. In this section, we establish the connection between these previous calculations and the analysis of the preceeding sections.

Guided by § 3.2, we make (2.1)–(2.3) dimensionless with respect to the scales

$$\hat{Z} = \left(\frac{K_c}{\Delta\rho\, g}\right)^{2/3}, \qquad \hat{P} = \Delta\rho\, g\hat{Z} = \frac{K_c}{\hat{Z}^{1/2}}, \qquad \hat{H} = \frac{\hat{P}\hat{Z}}{m}, \qquad \hat{T} = \frac{3\mu\hat{Z}}{\Delta\rho\, g\hat{H}^2} \tag{6.1}$$

to obtain

$$\frac{\partial H}{\partial T} = \frac{\partial}{\partial Z}\left(H^3\left(\frac{\partial P}{\partial Z} - 1\right)\right), \tag{6.2}$$

$$P(Z) = -\frac{1}{\pi}\int_0^\infty \frac{H'(S)}{S - Z}\,\mathrm{d}S, \tag{6.3}$$

$$H(Z) \sim (2(Z_n - Z))^{1/2} \quad \text{as } Z \to Z_n^-. \tag{6.4}$$

The variables in (6.2)–(6.4) are the same as, or direct analogues of, those used in the large-K analyses of §§ 4 and 5. We recall that the leading-order solution for steady propagation is a head of teardrop shape

$$H_0 = \tfrac{1}{2}X^{1/2}(2 - X)^{3/2}, \qquad 0 \leqslant X \equiv Z_n - Z \leqslant 2, \tag{6.5}$$

and dimensionless area $A_0 = \int_0^2 (2H_0)\,\mathrm{d}X = \pi/2$, which is attached to a tail of far-field width $K^{-4/3} \ll 1$. (The dimensional area is $\pi K_c^2/(2m\Delta\rho g)$.) We now seek the solution for a finite-volume release of area A.

As can be deduced from either (4.6) or equation (13) of Lister & Kerr (1991), if $A \leqslant A_0$ then it is possible to have a stationary crack in hydrostatic equilibrium provided that its vertical height 2ℓ satisfies $\ell^3 \leqslant A/A_0 \leqslant 2\ell^{3/2} - \ell^3$: if $A/A_0 > 2\ell^{3/2} - \ell^3$ then ℓ will increase by propagation at the top until equality is attained; if $A/A_0 < \ell^3$ then the fluid will drain upwards in the existing crack and collect in a teardrop-shaped region of half-height $\ell = (A/A_0)^{1/3}$. If, however, $A > A_0$ then there is no equilibrium shape and the crack must propagate upwards and continue to do so.

Spence & Turcotte (1990) neglect $\partial P/\partial Z$ in (6.2) and, omitting (6.3)–(6.4), obtain a similarity solution for propagation of a constant area A_t:

$$H = (Z/3T)^{1/2}, \qquad 0 < Z < (27A_t^2T/16)^{1/3}, \tag{6.6}$$

with a frontal shock of width $H_n(T) = (A_t/4T)^{1/3}$. (In dimensional terms, the solution for dimensional area α_t,

$$h = \left(\frac{\mu z}{\Delta\rho\, gt}\right)^{1/2}, \qquad 0 < z < \left(\frac{9\alpha_t^2\Delta\rho\, gt}{16\mu}\right)^{1/3}, \tag{6.7}$$

does not depend on either elasticity or fracture toughness.) The viscous–buoyancy balance in this solution is the same as that in the tail of the steadily propagating solution, and the rate of change of the frontal shock decreases with time. We thus anticipate that the frontal shock can be resolved at large times by matching to a quasi-steady teardrop-shaped head of the form (6.5). We equate the widths behind the head to obtain $K^{-4/3} = H_n(T)$ or

$$K(T) = \left(\frac{4T}{A_t}\right)^{1/4} = \left(\frac{4K_c^4 t}{\alpha_t m^3 \mu}\right)^{1/4}. \tag{6.8}$$

Since $K(T)$ increases in time, the solution in the head will tend to the large-K solution discussed in this paper, fed by a draining tail of area $A_t = A - A_0$. The rate of propagation is set by the tail area A_t and the head is quasi-steady for $T \gg A_t$.

In order to verify these ideas, the numerical method used by Roper & Lister (2005) to calculate propagation of a buoyant crack from an overpressured source was adapted to calculate propagation of a finite volume of fluid according to (6.2)–(6.4). Figure 8 shows the evolution of the crack shape from an initial elliptical shape with $A = 4A_0$. A head-and-tail structure has developed by the time $Z_n = 10$ and the head has a nearly constant shape of the form (6.5) for $Z_n \geqslant 20$. The draining tail tends towards the similarity form (6.6) for a volume $A_t = 3A_0$. The neck joining the head and the tail becomes shorter and more pronounced during propagation, owing to the increase in the effective value of K according to (6.8). There is very good agreement between the head and neck structure at $Z_n = 40$ and the steadily propagating solution for $K = 5.94$, which corresponds to (6.8) at $T = 1460$. On the basis of this numerical evidence, we conclude that when the flux from the tail is slowly varying, the solution in the head and neck has time to adjust to the slowly varying value of $K(T)$ and has the complicated structure of the steadily propagating crack.

Figure 9 confirms that the rate of propagation $\mathrm{d}Z_n/\mathrm{d}T$ is given asymptotically by (6.6), in particular in its dependence on $(A_t/T)^{2/3}$. This figure provides clear evidence that the rate of propagation is determined by the time-dependent flux in the draining tail and not by the head, which can adjust on a much shorter time scale; the flux from the tail is determined by a viscous–buoyancy balance in the tail, as in the theory of Spence & Turcotte (1990).

7. Discussion

7.1. *Structure of the steadily propagating solution for large K*

We have solved equations (2.7)–(2.9) for steady propagation fed by a constant flux using a mixture of asymptotic and numerical analysis. The solution has a rich asymptotic structure as $K \to \infty$, with the four major regions – head, neck, tail and distant tail – analysed in §§4 and 5 and Appendix B. As described below, and shown

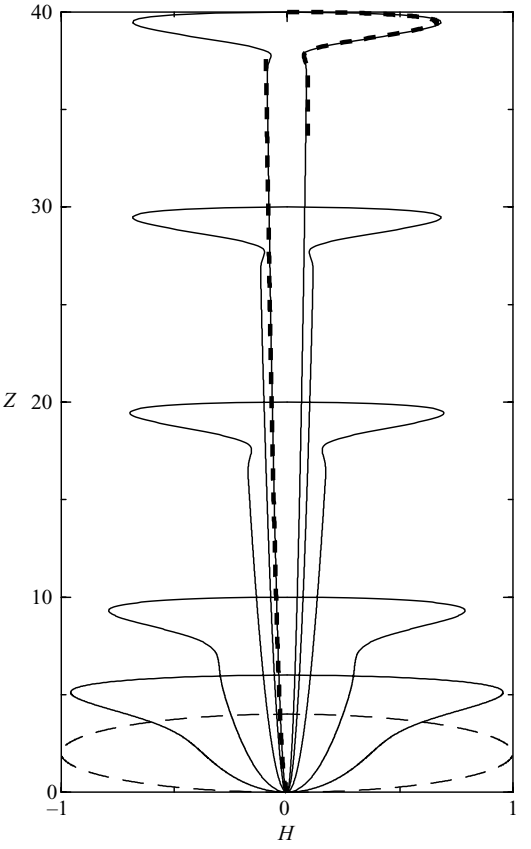

FIGURE 8. The evolution of the scaled crack width from an initial shape (long-dashed) $2H = [Z(4 - Z)]^{1/2}$ of volume $4A_0$, shown at $Z_n = 6$, 10, 20, 30 and 40. At $Z_n = 40$ the tail is well-described by the similarity solution (6.6) for $A_t = 3A_0$ and $Z = 38$ (bold dashed, on the left), which accounts for the length and volume of the head; the head is well-described by the steadily propagating solution for $K = 5.94$ (bold dashed, on the right), which corresponds to a tail width $H_\infty = 0.093$ behind the head. The calculation used 400 grid points.

schematically in figure 10, these major regions have up to eight different asymptotic subregions, distinguished by the behaviour of the non-locally determined pressure. This structure is a consequence of the two equations that couple p' and h: lubrication theory provides a local relationship between the pressure gradient p' and the width h, while elasticity provides an integral relationship between the width and the pressure distribution p along the whole crack. In the following description we revert to the variables h, p and x of (2.7)–(2.9), which are scaled on the far-field width rather than the fracture toughness.

Region Ia: the nose

The nose is the small subregion of the head where the viscous pressure gradient is significant owing to the narrow width near the crack tip. The fracture criterion gives a near-tip shape $h \sim K(2x)^{1/2}$. Lubrication theory then implies that $p' \sim (2K^2x)^{-1}$, giving a significant deviation from a hydrostatic gradient when $x \sim K^{-2}$. This is too small a region to have a significant effect on the width anywhere, despite the implied logarithmic singularity in p at $x = 0$.

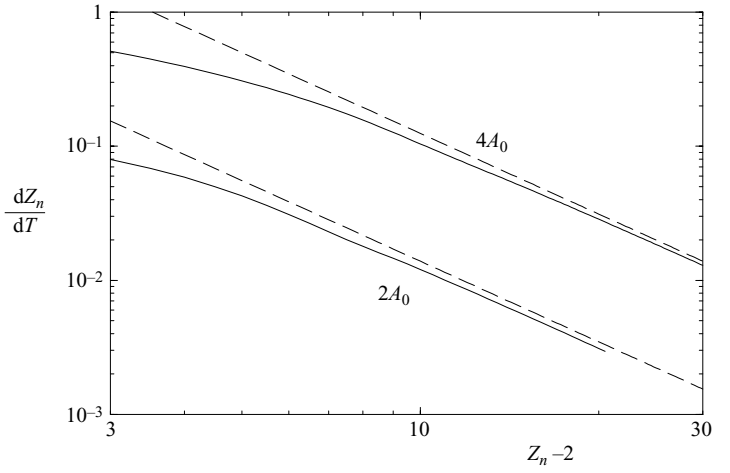

FIGURE 9. The propagation rate $\mathrm{d}Z_n/\mathrm{d}T$ as a function of the tail length Z_n-2 for the evolution from initial shapes $H=\frac{1}{2}[Z(4-Z)]^{1/2}$ and $H=\frac{1}{4}[Z(4-Z)]^{1/2}$ with volumes $A=4A_0$ and $2A_0$. After a transient the evolution tends towards the behaviour $\mathrm{d}Z_n/\mathrm{d}T=[3A_t/4(Z_n-2)]^2$ (dashed), predicted by (6.6), where $A_t=A-A_0$. The larger crack propagates 9 times faster than the smaller at a given length since the tail volumes are $3A_0$ and A_0, respectively. The crack propagates with a decreasing velocity governed by the tail and not at constant velocity governed by the head.

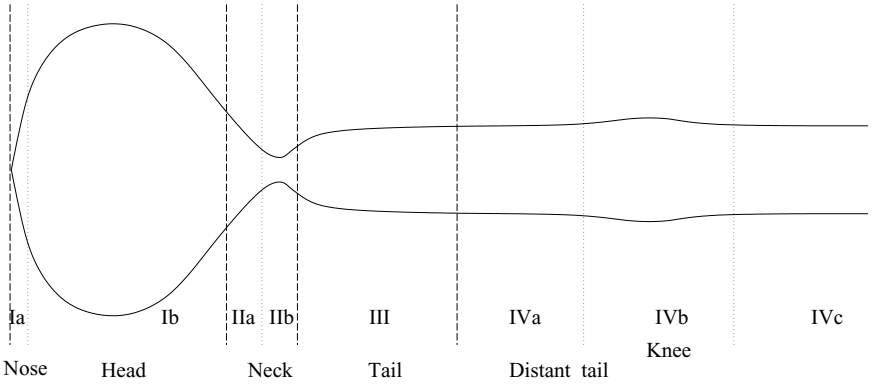

FIGURE 10. A schematic representation of the solution structure. The crack is divided into eight subregions as labelled. The scalings are: (Ia) $x \ll K^{-2}$ and $h=K(2x)^{1/2}$; (Ib) $x \sim K^{2/3}$ and $h \sim K^{4/3}$; (IIa) $(x-x_{\min}) \sim K^{-2/9}$ and $h \sim 1$; (IIb) $(x-x_{\min}) \sim K^{-2/5}$ and $h \sim K^{-4/15}$; (III) $x \sim K^{2/3}$ and $h \sim 1$; (IVa) $K^{2/3} \ll x \ll K^2$ and $h-1 \sim K^2 x^{-3}$; (IVb) $x \sim K^2$ and $h-1 \sim K^{-4}$; (IVc) $x \gg K^2$ and $h-1 \sim x^{-2}$.

Region Ib: the head

In order to generate a large stress intensity ahead of the crack tip, the crack is greatly inflated behind the tip. In this head region $h \gg 1$ which leads to $p'=-1$ and a leading-order balance between buoyancy and a hydrostatic elastic pressure. The hydrostatic gradient leads to a negative elastic pressure over the lower part of the head and the narrowing of the crack to form a teardrop shape given by (4.8). The length of the head is $O(K^{2/3})$ and the asymptotic width is $O(K^{4/3})$.

Region II: the neck

The neck matches the head to the tail. There are probably two subregions as described in §§ 5.1 and 5.2. In region IIa, we surmise that the base of the teardrop-shaped head is sufficiently narrow that the elastic–buoyancy balance is modified by viscous effects to give an $O(K^{-2/9})$ scale. The inner region IIb provides local elastic smoothing of the singularity in elastic pressure that would otherwise exist between the head and the tail. The scale of region IIb is $O(K^{-2/5})$ and the width at the minimum in the neck is $O(K^{-4/15})$.

Region III: the tail

In region III, an $O(K^{2/3})$ distance behind the head, there is a leading-order balance between buoyancy, the viscous pressure drop and elastic pressure. The elastic pressure is generated remotely by the large head, rather than by the $O(1)$ local width. The solution in the tail is given by (4.10).

Region IV: the distant tail

In the distant tail ($x \gg K^{2/3}$) there is a leading-order viscous–buoyancy balance and $h \approx 1$. The elastic pressure (B 2) gives a small correction to $h = 1$ according to (B 3): in region IVa ($K^{2/3} \ll x \ll K^2$) the correction is negative and $O(K^2 x^{-3})$ due to the elastic pressure from the head; in region IVc ($x \gg K^2$) the correction is positive and $O(x^{-2})$ due to the elastic pressure from the crack width at infinity. The two corrections are comparable in the knee region IVb, $x = O(K^2)$, where there is a local maximum (B 4).

7.2. *Geophysical and laboratory applications*

The dimensionless fracture toughness is defined as $K = K_c/\hat{K}$, where $\hat{K} = (3\mu Q m^3/2)^{1/4}$. The fracture toughness of the solid thus has a decreasing effect on the solution with increases in the flux of fluid, in the viscosity and particularly in the elastic modulus of the solid. Since the material parameters of laboratory analogues are very different from those in geophysical applications, this raises the question of whether the experiments are in the right dimensionless regime.

In geophysical situations, as pointed out by Lister (1990), the fracture-toughness scale is of order $\hat{K} \approx 10^8\,\mathrm{Pa\,m^{1/2}}$ (from $\mu = 100\,\mathrm{Pa\,s}$, $m = 10\,\mathrm{GPa}$ and $Q = 1\,\mathrm{m^2\,s^{-1}}$ e.g. $h_\infty = 1\,\mathrm{m}$, $\Delta\rho = 300\,\mathrm{kg\,m^{-3}}$). An order-of-magnitude variation in Q or μ changes $\hat{K}$ by less than a factor of 2, and m is less variable, though perhaps becomes more like 20 GPa. The value of K_c is open to some debate: laboratory measurements on rock cores suggest $K_c \approx 10^6\,\mathrm{Pa\,m^{1/2}}$ (see Atkinson 1984), but there are arguments (Rubin 1995) to suggest that the effective *in situ* value may be as large as $K_c \approx 10^8\,\mathrm{Pa\,m^{1/2}}$. This gives K in the range 0.01–1, though the larger values considered here would be appropriate for the later stages of a waning intrusion (cf. (6.8) for a fixed-volume release).

For laboratory analogues using fluids such as water or air and deformable solids such as gelatin or polyacrylamide gel, the scale $\hat{K}$ is such that the fracture toughness is always likely to be important. As a typical estimate for laboratory conditions, suppose that the half-width of the crack behind the head is $h_\infty = 0.5$–$1\,\mathrm{mm}$, the density contrast, for example between gelatin and water, is $\Delta\rho \approx 10\,\mathrm{kg\,m^{-3}}$ and the shear modulus, for example of gelatin (see Ito & Martel 2002), is $\approx 1\,\mathrm{kPa}$. These estimates together with the viscosity of water ($\mu = 10^{-3}\,\mathrm{Pa\,s}$) give fluxes of order $Q = 10^{-4}$–$10^{-5}\,\mathrm{m^2\,s^{-1}}$ and a fracture toughness scale $\hat{K} \approx 3\,\mathrm{Pa\,m^{1/2}}$. Any increase in μ will be compensated by a decrease in Q. The relationship between shear modulus and apparent fracture toughness for gelatin is discussed in Menand & Tait (2002) from which we estimate that $K_c \approx 100\,\mathrm{Pa\,m^{1/2}}$. This order of magnitude for K_c is supported

by the measurements of Heimpel & Olson (1994) who found fracture toughnesses of $K_c = 23\,\mathrm{Pa\,m^{1/2}}$ and $K_c = 114\,\mathrm{Pa\,m^{1/2}}$. The values above give K in the range 5–40. Laboratory experiments are thus in the regime $K \gg 1$, in which the fracture toughness has a significant influence on the shape of the solution. This estimate of the dimensionless parameter regime, together with our detailed analysis, provides a theoretical explanation for the common experimental observations of bulbous heads and much thinner tails. It also points out that many of the experiments designed to investigate geophysical situations may not be in the right parameter regime. Owing to the one-quarter power in the definition of $\hat{K}$, it is not easy to change K by an order of magnitude.

We are aware of only a few experimental studies that provide quantitative measurements on propagation rates in gelatin that might be compared with the theory in this paper. In part, this is because many experiments (e.g. Fiske & Jackson 1972; Muller *et al.* 2001; Ito & Martel 2002) are designed to investigate dyke paths in varying stress fields and, in part, because it is difficult to measure crack widths (especially in the tail) and the lateral extent of the three-dimensional crack is often not reported. The most relevant of the experimental studies are by Takada (1990) and Heimpel & Olson (1994), which describe vertical propagation of buoyant cracks of fixed volume, analogous to the calculations in § 6. Clear head-and-tail structures are reported with a lateral extent comparable to the height of the head. There is some evidence of viscous control of propagation rate in observations of increasing propagation rates in a given gel with decreasing-viscosity fluids (figure 10 in Takada (1990) and the 1.6 %-gelatin data in figure 2 of Heimpel & Olson (1994)), though not with the simple proportionality to $\Delta\rho/\mu$ suggested by (2.1); it should be noted that variations in $\Delta\rho$ between fluids would also have affected the head height and volume.

Moreover, there are indications in the data of Heimpel & Olson (1994) that the fracture criterion in gelatin may not, in fact, be given by the simple fracture toughness K_c of a brittle linear elastic solid. There is no analytical solution for a 'three-dimensional Weertman pulse' (with stress intensity equal to K_c along its upper boundary and on the point of closing along its lower boundary), but a numerical solution would be expected to have the same scalings as (6.5) with vertical and lateral extent $O((K_c/\Delta\rho\, g)^{2/3})$ and width $O((K_c/\Delta\rho\, g)^{1/3} K_c/m)$, thus giving a critical volume $V_0 = O((K_c/\Delta\rho\, g)^{5/3} K_c/m)$. Without needing to take a view on the detailed scalings for such a pulse or on the effect of viscosity on propagation rate, consideration of a simple fracture toughness criterion suggests, first, that a buoyant crack with volume less than V_0 should not propagate and, secondly, that a crack with low viscosity and large toughness should propagate with a head of approximately the fixed shape and volume of such a pulse. Figures 2 and 3 of Heimpel & Olson (1994) conflict with both predictions: first, the propagation rate decreases rapidly with decreasing injected volume, but does not appear to tend to zero at an identifiable V_0; secondly, the size of the head increases markedly with increasing total injected volume, rather than being approximately fixed. These observations suggest that the failure mechanisms in gelatin, a soft polymeric network of gelling agent that traps the water, are significantly different from those of more rigid brittle solids such as ceramics or rock. In particular, they suggest a rate-dependent fracture resistance.

7.3. *Conclusion*

Buoyancy-driven crack propagation occurs in the regime of large fracture toughness in laboratory experiments, in the later stages of ascent of a finite pulse of magma, and probably in other geological situations if the *in situ* fracture toughness of rocks is much greater than laboratory measurements suggest. The asymptotic structure for

large fracture toughness is complicated and some fine details of the structure of the neck are not yet completely understood. However, the dynamics that determine the shape of the head, the tail and the rate of propagation have now been elucidated through solutions to the canonical problems of steady propagation with a fixed flux and of time-dependent propagation of a fixed volume of fluid. The same principles and dynamic balances will also apply to other source conditions in the large-toughness regime.

At large fracture toughness, the head is much wider than the tail, viscous pressure drops in the head are negligible, and the head thus has the teardrop shape derived by Weertman (1971*a*) for a hydrostatic crack on the point of propagating. However, the inferences, which recur in some of the geophysical literature, that viscosity is unimportant or that such a teardrop-shaped pulse of magma should propagate at a constant velocity because it has a constant shape are both incorrect. As shown in § 6, the rate of propagation is determined by the time-dependent flow in the much thinner tail, where the dominant balance is between buoyancy and viscosity. When the tail is much longer than the head, the propagation rate is given by the average velocity *behind* the head, $\Delta\rho g h_n^2/3\mu$, where h_n is the half-width a few headlengths behind the head and neck. The value of $h_n(t)$ is itself determined by the viscous–buoyancy drainage dynamics in the rest of the tail under which disturbances propagate away from the source towards the head as described by Spence & Turcotte (1990). The effective dimensionless fracture toughness, assumed large, is given by $K = K_c/(\Delta\rho\, g h_n^3 m^3)^{1/4}$, which will evolve with h_n. It is hoped that an understanding of these dynamics and scalings will, in particular, guide the interpretation of laboratory simulations and allow their design to be for the appropriate dimensionless regime.

Appendix A. Numerical schemes

The numerical method of Lister (1990) was adapted to solve (3.2). For calculations with $K \leqslant 256$ we set $F = P'X(1 + X)$ and $X = \tan^2 Y$. We approximated $F(Y)$ by a piecewise linear function on N panels ($N+1$ grid points) which partition $0 \leqslant Y \leqslant \pi/2$. The grid points were distributed on a non-uniform but smoothly varying grid chosen such that more points were placed around the neck region, while maintaining good resolution elsewhere, as K increases. The lubrication equation was represented at the $N-1$ interior points, the asymptotic value $F = (2K^{8/3})^{-1}$ imposed at the crack tip and the stress-intensity condition (3.2*c*) used to close the system. A Newton method was used to solve this nonlinear system of $N+1$ equations for the values of F. A simple initial guess gave rapid convergence of the method for $K = 1$. A continuation scheme was used to obtain a sequence of solutions for larger values of K: the solution for $K = K_i$ was mapped onto the grid for $K = K_{i+1} > K_i$ by interpolation and then used as the initial guess for the Newton solution with $K = K_{i+1}$. This also gave rapid convergence with, for example, $K_{i+1}/K_i = 2^{1/4}$.

For very large values of K there are problems resolving in addition the $O(K^{-8/3})$ scale of the near-tip singularity and the $O(K^{4/3})$ scale of the far-field tail. To avoid these problems when examining the detailed structure of the neck in § 5 for $K > 256$, it was found advantageous to restrict the numerical domain from $X \in [0, \infty)$ to $[a, b]$, and to make use of the asymptotic solutions for P from § 4 and Appendix B in the regions $[0, a)$ and (b, ∞). We set $P' = -1$ for $X \leqslant a$ and $P' = \gamma P_0' - (\pi K^{4/3} X^2)^{-1}$ for $X \geqslant b$, where γ is to be determined as part of the solution. The errors in these approximations have a negligible effect on the solution in the neck.

With this assumed form for the pressure, (3.2*b*, *c*) become

$$H(X) = H_a + \gamma H_b + \frac{H_\infty}{K^{4/3}} + \frac{1}{\pi}\int_a^b k(S, X)P'(S)\,\mathrm{d}S, \tag{A 1}$$

$$\frac{\pi}{\sqrt{8}} - \frac{2a^{3/2}}{3} - \frac{2}{\pi K^{4/3}b^{1/2}} + \gamma\int_b^\infty S^{1/2}P_0'\,\mathrm{d}S + \int_a^b S^{1/2}P'\,\mathrm{d}S = 0, \tag{A 2}$$

where

$$H_a = -\frac{1}{\pi}\int_0^a k(S, X)\,\mathrm{d}S = \frac{a^2}{\pi}\left(\frac{X}{a}\right)^{1/2}\left(\frac{5}{3} - \frac{X}{a}\right) + \frac{a^2}{2\pi}\left(\frac{X}{a} - 1\right)^2 \log\frac{(X/a)^{1/2}+1}{(X/a)^{1/2}-1}, \tag{A 3a}$$

$$H_b = \frac{1}{\pi}\int_b^\infty k(S, X)P_0'(S)\,\mathrm{d}S = \sum_{i=3}^{\infty}\frac{c_i}{\pi}\int_b^\infty S^{-i}k(S, X)\,\mathrm{d}S, \tag{A 3b}$$

$$H_\infty = -\frac{1}{\pi^2}\int_b^\infty \frac{1}{S^2}k(S, X)\,\mathrm{d}S = -\frac{1}{2} + \frac{2}{\pi^2}\int_1^{(b/X)^{1/2}}\frac{1}{t}\log\frac{1+t}{t-1}\,\mathrm{d}t - \frac{k(b, X)}{b\pi^2}, \tag{A 3c}$$

and $k(S, X)$ is given in (2.11). The integrals in (A 3*b*) can be done analytically and that in (A 3*c*) is found using NAG library routines. The coefficients c_i are obtained from the binomial expansion of $P_0'(S)$ in powers of S^{-1} which converges in $S > 2$; we included terms up to c_{18} for $b = 5$.

On the truncated domain we used the lubrication equation at the $N+1$ grid points together with (A 2) to solve for the $N+1$ values of P' and γ using a Newton method; continuation with K and grid-point redistribution were used as above. Good convergence starting with $K = 5$ was found using $a = 1$ and $b = 5$, and good agreement was obtained with solutions from the untruncated scheme for $K > 100$. The truncated scheme was used to calculate solutions up to $K = 3600$ with the number of points increasing from about $N = 700$ for $K = 5$ to $N = 2000$ for $K = 3600$ in order to maintain good resolution in the neck.

Appendix B. The distant tail, $X = O(K^{4/3})$

As $X \to \infty$ the half-width in the tail tends to the constant value $K^{-4/3}$ and it seems likely that the influence of the distant head should become negligible. As in Spence *et al.* (1987), the integral equation (2.8) can be developed as a power series in x^{-1} to give, after rescaling,

$$P = \frac{H(\infty) - H(0)}{\pi X} - \frac{1}{\pi X^2}\int_0^\infty (H - H(\infty))\,\mathrm{d}S + O\left(\frac{H}{X^3}\right) \tag{B 1}$$

where $H(0) = 0$ and $H(\infty) = K^{-4/3}$. For $K \gg 1$, $\int_0^\infty H - H(\infty)\,\mathrm{d}S \approx \int_0^2 H_0\,\mathrm{d}S = \pi/4$ and thus

$$P \approx \frac{1}{K^{4/3}\pi X} - \frac{1}{4X^2} + O\left(\frac{H}{X^3}\right). \tag{B 2}$$

The second term in (B 2) is the leading-order term in the expansion of $P_0(X)$ for $X \gg 1$, and the first originates from the fact that $H(\infty)$ is $K^{-4/3}$ and not zero; the two terms are comparable when $X = O(K^{4/3})$. Thus for $X \gg K^{4/3}$ the pressure in the tail is dominated by the effect of the non-zero width at infinity, and for $2 \leqslant X \ll K^{4/3}$ the pressure is dominated by the contribution from the head.

Using (3.2a) for $X \gg 1$, we linearize H^{-2} about $H = H(\infty)$ and rearrange to obtain

$$H \approx \frac{1}{K^{4/3}} \left(1 - \frac{P'}{2}\right). \tag{B 3}$$

Substitution of (B 2) into (B 3) shows that there is a local maximum, or 'knee', in H given by $P'' = 0$. The knee is at

$$X_m = \frac{3\pi K^{4/3}}{4} \quad \text{and} \quad H(X_m) \sim \frac{1}{K^{4/3}} \left(1 + \frac{8}{27\pi^3 K^4}\right). \tag{B 4}$$

These details of the solution for $X = O(K^{4/3})$ are too far away to have a significant effect on the head and neck.

Appendix C. Difficulties in posing an inner problem for the neck

In § 5 we showed good collapse of numerical solutions in the neck region with $H \sim K^{-8/5}$ and $X - X_{\min} \sim K^{-16/15}$. To fully determine the solution in the neck, we should formulate an inner problem using these scalings, with matching conditions to the head and the tail. It might, at first sight, be thought that the problem is similar to the classic Bretherton analysis (Bretherton 1961) of a long bubble in a narrow tube, with the head loosely analogous to the static region ahead of the bubble, the tail to the thin film along the length of the bubble and the neck to the short region that matches the two. However, a major difference between the problems is that the elastic pressure is determined non-locally by an integral equation, whereas the capillary pressure is given by the local curvature. The non-local character of the elastic pressure causes difficulties in formulating an inner problem that we have been unable to overcome.

Suppose we define an inner variable $\xi = (X - X_{\min})K^{16/15}$. To match to the head and the tail, we would expect the inner solution to have the properties that $H \to (-\xi)^{3/2}$ as $\xi \to -\infty$ and $H \to \xi^{1/4}$ as $\xi \to \infty$. However it is not clear how to impose these limits or if they are a consequence of some other condition. The behaviour $(-\xi)^{3/2}$ at the base of the head, rather than the more generic $(-\xi)^{1/2}$, is a consequence of the correct balance of positive and negative pressure in $0 \leqslant X \leqslant 2$. This balance of pressures also gives that $P_0' \sim \xi^{-1/2}$ and not $P_0' \sim \xi^{-3/2}$ for $\xi \geqslant 0$, which in turn gives $H \sim \xi^{1/4}$. Both matching conditions for H are thus determined non-locally by the pressure distribution on the $O(1)$ length scale of X and it is not clear how to formulate a local condition on the $O(K^{-16/15})$ length scale of ξ.

It is worth noting that there is also the possibility of a double inner layer, though the numerical evidence for this is ambiguous. The discussion in § 5.2 suggests that there may be a modification to the asymptotic solutions not only on the scale of $K^{-16/15}$ but also on the larger scale of $K^{-8/9}$. Thus matching to the behaviour $H \sim (2 - X)^{3/2}$ in the head may only be achievable through this second scale.

REFERENCES

Anderson, O. L. 1978 The role of magma vapours in volcanic tremors and rapid eruptions. *Bull. Volcanol.* **41**, 341–353.

Andrews, J. R. & Emelius, C. H. 1975 Structural aspects of kimberlite dyke and sheet intrusion in south-west Greenland. *Phys. Chem. Earth* **9**, 43–50.

Atkinson, B. K. 1984 Subcritical crack growth in geological materials. *J. Geophys Res.* **89**, 4077–4114.

Bretherton, F. P. 1961 Motion of long bubbles in tubes. *J. Fluid Mech.* **10**, 166–188.

Delaney, P. T., Pollard, D. D., Ziony, J. I. & McKee, E. H. 1986 Field relations between dikes and joints: emplacement processes and paleostress analysis. *J. Geophys. Res.* **91**, 4920–4938.

Detournay, E. 2004 Propagation regimes of fluid-driven fractures in impermeable rocks. *Intl J. Geomech.* **4**, 1–11.

Erdelyi, A., Magnus, W., Oberhettinger, F. & Tricomi, F. G. (Eds.) 1954 *Tables of Integral Transforms.* McGraw Hill.

Fialko, Y. A. & Rubin, A. M. 1997 Numerical simulation of high-pressure rock tensile fracture experiments: Evidence for an increase in fracture energy with pressure? *J. Geophys. Res.* **102**, 5231–5242.

Fiske, R. S. & Jackson, E. D. 1972 Orientation and growth of hawaiian volcanic rifts: the effect of regional structure and gravitational stresses. *Proc. R. Soc. Lond.* A **329**, 299–326.

Garagash, D. I. 2006 Plane-strain propagation of a fluid-driven fracture during injection and shut-in: Asymptotics of large toughness. *Engng Fracture Mech.* **73**, 456–481.

Geertsma, J. & Haafkens, R. 1979 A comparison of the theories for predicting width and extent of vertical hydraulically induced fractues. *J. Energy Resour. Tech.* **101**, 8–19.

Heimpel, M. & Olson, P. 1994 Buoyancy-driven fracture and magma transport through the lithosphere: Models and experiments. *Magmatic Syst.* **57**, 223–240.

Irwin, G. R. 1958 Fracture. In *Handbuch der Physik*, vol. 6, pp. 551–590. Springer.

Ito, G. & Martel, S. J. 2002 Focusing of magma in the upper mantle through dike interaction. *J. Geophys. Res.* **107** (B10), 2223.

Kanninen, M. F. & Popelar, C.H. 1985 *Advanced Fracture Mechanics*. Oxford University Press.

Lawn, B. R. & Wilshaw, T.R. 1975 *Fracture of Brittle Solids*. Cambridge University Press.

Lister, J. R. 1990 Buoyancy-driven fluid fracture: the effects of material toughness and of low-viscosity precursors. *J. Fluid Mech.* **210**, 263–280.

Lister, J. R. 1994*a* The solidification of buoyancy-driven flow in a flexible-walled channel. Part 1. Constant-volume release. *J. Fluid Mech.* **272**, 21–44.

Lister, J. R. 1994*b* The solidification of buoyancy-driven flow in a flexible-walled channel. Part 2. Continual release. *J. Fluid Mech.* **272**, 45–65.

Lister, J. R. & Kerr, R. C. 1991 Fluid-mechanical models of crack propagation and their application to magma-transport in dykes. *J. Geophys. Res.* **96**, 10049–10077.

Menand, T. & Tait, S. R. 2002 The propagation of a buoyant liquid-filled fissure from a source under constant pressure: An experimental approach. *J. Geophys. Res.* **107** (B11), 2306.

Mériaux, C., Lister, J. R., Lyakhovsky, V. & Agnon, A. 1999 Dyke propagation with distributed damage of the host rock. *Earth Planet. Sci. Lett.* **165**, 177–185.

Muller, J. R., Ito, G. & Martel, S. J. 2001 Effects of volcano loading on dike propagation in an elastic half-space. *J. Geophys. Res.* **106** (B6), 11101–11113.

Pollard, D. D. 1987 Elementary fracture mechanics applied to the structural interpretation of dykes. In *Mafic Dyke Swarms* (ed. H. C. Halls & W. H. Fahrig). Geol. Soc. Canada Special Paper 34.

Roper, S. M. & Lister, J. R. 2005 Buoyancy-driven crack propagation from an over-pressured source. *J. Fluid Mech.* **536**, 79–98.

Rubin, A. M. 1993 Tensile fracture at high confining pressure: Implications for dike propagation. *J. Geophys. Res.* **98**, 15919–15935.

Rubin, A. M. 1995 Propagation of magma-filled cracks. *Annu. Rev. Earth Planet. Sci.* **23**, 287–336.

Rubin, A. M. 1998 Dyke ascent in partially molten rock. *J. Geophys. Res.* **103**, 20901–20919.

Rubin, A. M. & Pollard, D. D. 1987 Origins of blade-like dikes in volcanic rift zones. *US Geol. Surv. Prof. Paper* 1350, pp. 1449–1470.

Ruina, A. L. 1978 Influence of coupled deformation-diffusion effects on the retardation of hydraulic fracture. *Proc. 19th US Symp. Rock Mechanics* (ed. Y. S. Kim), pp. 274–282. University of Nevada-Reno.

Spence, D. A., Sharp, P. & Turcotte, D. L. 1987 Buoyancy-driven crack propagation: a mechanism for magma migration. *J. Fluid Mech.* **174**, 135–153.

Spence, D. A. & Turcotte, D. L. 1990 Buoyancy-driven magma fracture: a mechanism for ascent through the lithosphere and the emplacement of diamonds. *J. Geophys. Res.* **95** (B4), 5133–5139.

Stevenson, D. J. 1982 Migration of fluid-filled cracks: applications to terrestrial and icy bodies. *Lunar Planet. Sci.* **XIII**, 768–769.

Takada, A. 1990 Experimental study on propagation of liquid-filled crack in gelatin: Shape and velocity in hydrostatic stress condition. *J. Geophys. Res.* **95**, 8471–8481.

Valko, P. & Economides, M. J. 1995 *Hydraulic Fracture Mechanics*. Wiley.

Weertman, J. 1971*a* Theory of water-filled crevasses in glaciers applied to vertical magma transport beneath oceanic ridges. *J. Geophys. Res.* **76**, 1171–1183.

Weertman, J. 1971*b* Velocity at which liquid-filled cracks move in the Earth's crust or in glaciers. *J. Geophys. Res.* **76**, 8544–8553.